Journal of Magnetic Resonance 265 (2016) 99–107

Contents lists available at ScienceDirect

Journal of Magnetic Resonance

journal homepage: www.elsevier.com/locate/jmr

Improvement of the Off-Resonance Saturation, an MRI sequence for positive contrast with SPM particles: Theoretical and experimental study

S. Delangre [a], Q.L. Vuong [a], C. Po [b], B. Gallez [b], Y. Gossuin [a,*]

[a] Biomedical Physics Unit, Université de Mons, Place du Parc 20, 7000 Mons, Belgium
[b] Biomedical Magnetic Resonance Research Group, Louvain Drug Research Institute, Université Catholique de Louvain, Brussels, Belgium

ARTICLE INFO

Article history:
Received 20 July 2015
Revised 2 February 2016
Available online 9 February 2016

Keywords:
Magnetic resonance imaging
Positive contrast imaging
Off-resonance imaging
Iron oxide nanoparticles
Superparamagnetic nanoparticles
Contrast agents

ABSTRACT

The SuperParaMagnetic particles (SPM particles) are used as contrast agents in MRI and produce negative contrast with conventional T_2 or T_2^*-weighted sequences. Unfortunately, the SPM particle detection on images acquired with such sequences is sometimes difficult because negative contrast can be created by artifacts such as air bubbles or calcification. To overcome this problem, new sequences as Off-Resonance Saturation (ORS) were developed to produce positive contrast with SPM particles. This work explores a new way to optimize the contrast generated by the ORS sequence by increasing the number of saturation pulses applied before the imaging sequence. This modified sequence is studied with numerical simulations and experiments on agarose gel phantoms. A theoretical model able to predict the contrast for different values of the sequence parameters is also developed. The results show that the contrast increases with the saturation pulses number with an optimal value of three saturation pulses in order to avoid artifacts and limit the Specific Absorption Rate (SAR) effect. The dependence of the contrast on the SPM particle concentration and sequence parameters is comparable to what was observed for the ORS sequence.

1. Introduction

Magnetic Resonance Imaging (MRI) is a powerful medical imaging technique providing images with an excellent resolution and a good intrinsic contrast [1–4]. However, the use of contrast agents (CA) is sometimes needed to highlight specific regions such as tumors [5,6].

The iron oxide SuperParaMagnetic particles (SPM particles) are one kind of CA used in MRI. These magnetic particles decrease T_2 and T_2^* in their surroundings and have a negligible effect on T_1 at high magnetic field [7–9]. Therefore, they are usually used as negative MRI contrast agents with conventional T_2 or T_2^*-weighted sequences [9–11].

The SPM particles advantages are their non-toxicity and their functionalizable surface. Thanks to these features, they are widely used in molecular and cellular imaging [12–16] but also for applications such as hyperthermia [17], tumors targeting [18,19] and drug delivery therapy followed by MRI [20,21].

Unfortunately, the SPM particle detection in MR images is sometimes difficult. Indeed negative contrast is not only produced by the SPM particles but also by artifacts such as air bubbles or calcifications in T_2 or T_2^*-weighted MR images. To overcome this problem, new MR imaging sequences producing positive contrast with SPM particles were developed in these last years [22–24].

The positive contrast methods can be divided in four category: (1) Sequences using frequency selective pulses before/during the imaging sequence. The ON-Resonance Saturation (ONRS) [25–27], the Off-Resonance Saturation (ORS) [28–31] and the Off-Resonance Imaging (ORI) [32–34] sequences belong to this category. (2) Sequences using an off-resonance shift during the sequence acquisition, as the GRASP [35–38] or the co-RASOR techniques [39]. (3) Sequences using a specific post-processing image reconstruction, as the phase gradient imaging [40,41] or the susceptibility weighted imaging [42,43]. (4) Sequences using ultrashort echo times [44,45].

In this work, we propose to modify the ORS sequence in order to improve the positive contrast generated by this sequence. The classical ORS sequence principle is to subtract two MR images obtained with the same imaging sequence: one with and one without the application of an off-resonance saturation pulse before the imaging

* Corresponding author at: Biomedical Physics Department, University of Mons, Avenue du champ de mars, 24, 7000 Mons, Belgium.
E-mail address: yves.gossuin@umons.ac.be (Y. Gossuin).

http://dx.doi.org/10.1016/j.jmr.2016.02.002
1090-7807/

sequence [31]. The ORS sequence was extensively studied in our previous work [31], which provides a theoretical understanding of the mechanism leading to the positive contrast. The present work shows that the contrast can be significantly increased if several saturation pulses are used before the imaging sequence. First the theoretical model reported in [31] was extended to describe the contrast generated by the modified ORS sequence using several saturation pulses. Numerical simulations and experiments on agarose gels containing SPM particles were performed to study the modified ORS sequence. The theoretical predictions were then compared to the simulation and experimental results. Moreover the influence on the contrast of the SPM particle concentration, the number of saturation pulses and the saturation pulse parameters was investigated.

2. Theory

This work aims to improve the contrast generated by the ORS sequence. To this purpose, several saturation pulses were applied before the imaging sequence, while only one saturation pulse is used in the classical ORS sequence. In this section, the ORS sequence principle is first described. A theoretical description of the modified ORS sequence is then provided.

2.1. ORS principle and theory

The ORS principle was described in [28,31]. At high magnetic field, a SPM particle can be considered as a magnetic dipole aligned with the main magnetic field of the MRI scanner $\vec{B}_0$ (aligned with the z axis). Its dipolar moment is saturated if $B_0 > 0.5$ T [7]. A SPM particle creates a dipolar magnetic field whose longitudinal component (the transverse components are negligible if B_0 is high enough) is given by

$$B_{dip} = \frac{B_{eq}R_P^3}{r^3}(3\cos^2\theta - 1). \quad (1)$$

In this equation, R_P is the particle radius, $\vec{r}$ is the vector connecting the SPM particle center to the considered position, θ is the angle between $\vec{B}_0$ and $\vec{r}$, and $r = |\vec{r}|$. B_{eq} is the SPM particle equatorial field (expressed in Tesla), defined as the field magnitude at the particle equator. Its value is proportional to the particle magnetization M_S, expressed as A m^2/kg [Fe] (see Eq. (1) in [27]):

$$B_{eq} = 1245\mu_0 M_S, \quad (2)$$

with μ_0 the magnetic permeability of the vacuum.

The magnetic field created by the SPM particle induces a Larmor frequency shift of the water protons in the SPM particle surroundings. The ORS sequence takes advantage of the broadening of the distribution of proton Larmor frequencies, caused by the SPM particles, to produce positive contrast near the particles. The final image is obtained by subtracting two MR images: one acquired without and one with the application of a frequency selective saturation pulse before the image acquisition sequence. The saturation pulse parameters, i.e. its bandwidth $\Delta\omega$ and its frequency offset ω_0, are chosen in order to spoil only the MR signal created by the protons near the SPM particles. The subtraction of these two images results in a positive contrast in the region containing the SPM particles (see Fig. 2 in [31] for more details).

The contrast induced by an ORS sequence using a Fast Imaging with Steady-state free Precession (FISP) image acquisition sequence [1–3,46–48] was theoretically studied in [31]. This reference provides an analytical equation of the contrast:

$$C = \Phi(\omega_0, \Delta\omega, B_{eq}, Cc)\sin\alpha M_z^0 e^{-TE(r_2^* Cc + R_2^*)}. \quad (3)$$

In this equation,

$$\Phi(\omega_0, \Delta\omega, B_{eq}, Cc) = \frac{1}{\pi}\left[\arctan\left(\frac{1.32\cdot 10^{-3}}{B_{eq}Cc}(\omega_0 + \Delta\omega/2)\right) - \arctan\left(\frac{1.32\cdot 10^{-3}}{B_{eq}Cc}(\omega_0 - \Delta\omega/2)\right)\right]$$

is the fraction of protons saturated (spoiled) by the saturation pulse, Cc is the iron concentration (expressed in mM [Fe]), α is the flip angle of the FISP sequence excitation pulse, M_z^0 is the longitudinal component of the SPM equilibrium magnetization, TE is the echo time, r_2^* is the proton transverse relaxivity induced by the SPM particles (defined as the increase of the relaxation rate R_2^* when the iron concentration increases of 1 mM) and R_2^* is the intrinsic transverse relaxation rate of the solvent containing the SPM particles. Eq. (3) shows that the contrast is proportional to Φ.

2.2. ORS improvement

In this work, we improve the contrast generated by ORS by applying several saturation pulses before the imaging sequence. This procedure affects the contrast only through the fraction of saturated protons Φ because all the saturation pulses are applied before the imaging sequence (Fig. 1).

Fig. 2 shows that a higher number of saturation pulses N_{Sat} can increase the fraction of saturated protons. As the contrast is proportional to the fraction of saturated protons (Eq. (3)), the contrast must thus increase with N_{Sat}. To theoretically describe this phenomenon, let us suppose that the water proton diffusion is fast enough to have a homogeneous solution of saturated and unsaturated protons before the application of the next saturation pulse. This condition is satisfied if the inequation

$$\tau_D < \frac{24\Delta t_{Sat}}{(4\pi 67\cdot 10^3/3Cc)^{2/3}}, \quad (4)$$

is verified (see Section 1 of the supplementary materials for more details). In Eq. (4), Δt_{Sat} is the time interval between each saturation pulse (Fig. 1), $\tau_D = R_P^2/D$ is the water proton correlation time, with D the protons diffusion coefficient and R_P the SPM particles radius (if the SPM particles are clustered, R_P is the radius of the clusters). For example, for SPM particles in water with $R_P = 5$ nm and $Cc = 1$ mM, $\Delta t_{Sat} > 6$ μs. In other media characterized by smaller diffusion coefficients than water, Δt_{Sat} will increase. Table 1 provides some estimations of Δt_{Sat} for agar gel, cartilage, muscle and bone marrow. We can thus consider than in most of the cases, the "mixing" condition is fulfilled since in practice Δt_{Sat} is of the order of 5 ms which is far larger than the values reported in Table 1. This also means that the value of Δt_{Sat} won't influence the fraction of saturated protons and the contrast as far as the longitudinal relaxation is neglected during the saturation pulse train. This last assumption is justified by the large T_1 of our samples ($T_1 \geqslant 0.5$ s) compared to the saturation pulse train duration, which is equal to $\Delta t_{Sat}N_{Sat}$ and always smaller than 25 ms in this study while the total time needed for the acquisition of an image is about 0.5 s.

If we consider a saturation pulse train of N_{Sat} saturation pulses, the first excitation pulse saturates a fraction Φ of protons situated in the area affected by the saturation pulses (Fig. 2). If condition (4) is fulfilled, the second saturation pulse saturates a fraction $\Phi_1 = \Phi(1-\Phi)$ of protons unsaturated by the first saturation pulse (Fig. 2). Therefore, the total fraction of protons saturated after the second saturation pulse, written as Φ_2, is given by

$$\begin{aligned}\Phi_2 &= \Phi_1 + \Phi(1-\Phi_1)\\ &= 1-(1-\Phi)^2\end{aligned}. \quad (5)$$

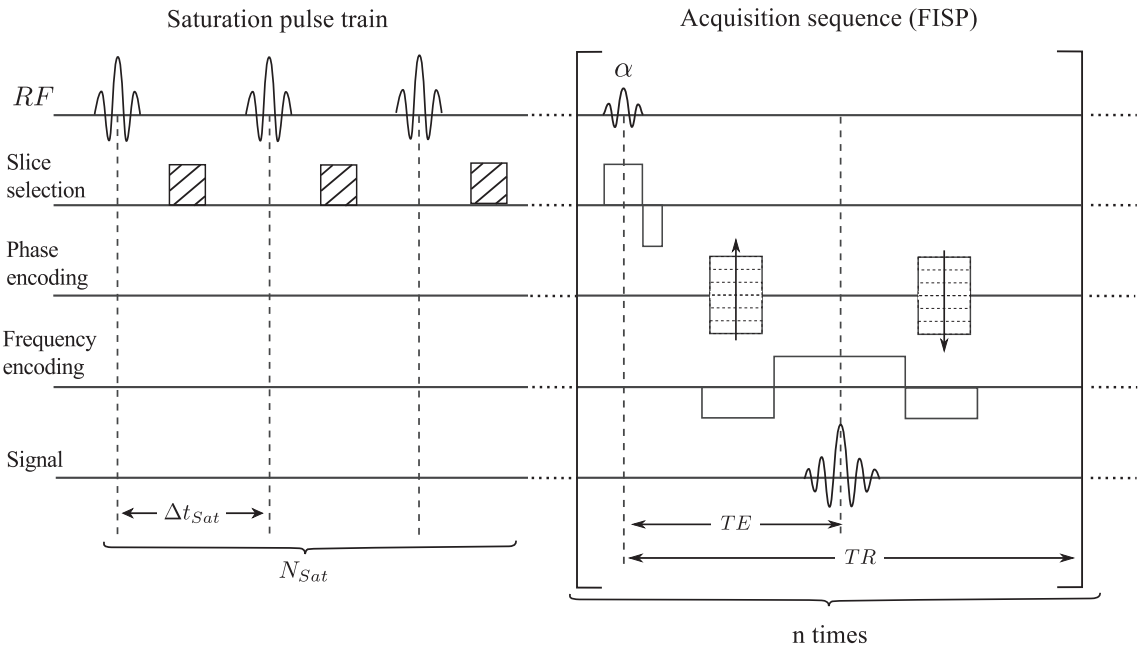

Fig. 1. Modified ORS sequence. A saturation pulses train is applied before the imaging sequence acquisition (FISP). All the saturation pulses have a bandwidth tuned to saturate only the protons situated near the SPM particles, and are followed by a spoiler gradient.

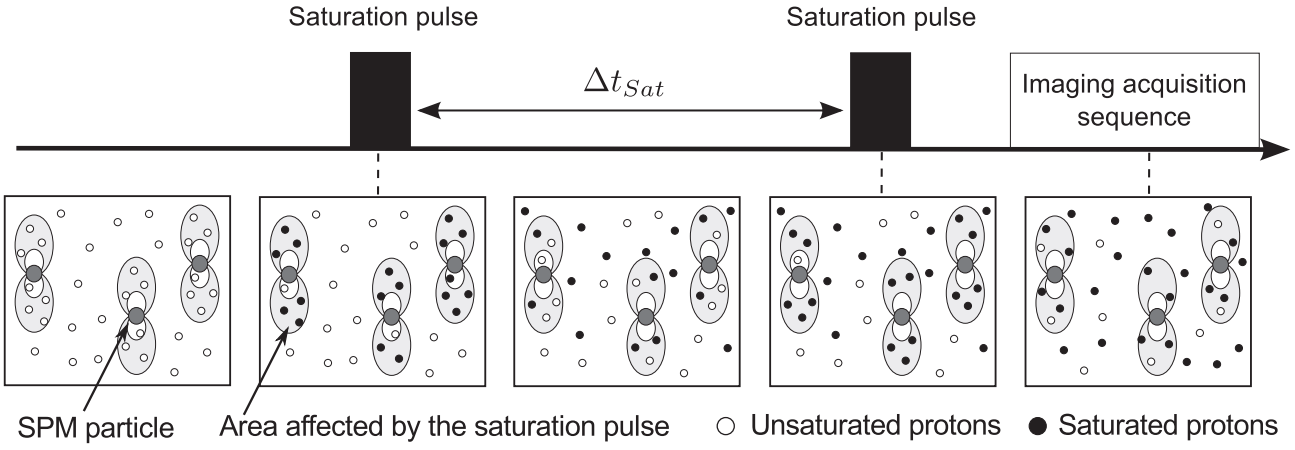

Fig. 2. Animation of the effect of several saturation pulses on the fraction of saturated protons. The first saturation pulse saturates all the protons situated near the SPM particles (light gray areas). Thanks to proton diffusion, the unsaturated and the saturated protons are mixed together before the application of the second saturation pulse. Therefore, this second pulse saturates some protons that were not saturated by the first pulse. The total fraction of saturated protons is thus increased.

Table 1
Estimations of minimum Δt_{Sat} values for an optimal mixing of the protons between saturation pulses, for different media.

Media	Diffusion coefficient (10^{-9} m^2/s)	Minimum Δt_{Sat} (μs)
Water	3	6
Agar gel [49]	1.8–2.2	8.2–10
Cartilage [50]	0.68–1.45	12–26
Muscle [51]	1.8	10
Bone marrow [52]	0.15	120

If we apply this argument for N_{Sat} pulses, we find

$$\Phi_{N_{Sat}} = 1 - (1 - \Phi)^{N_{Sat}}. \quad (6)$$

Eq. (6) shows that the fraction of saturated protons increases with N_{Sat}. At low iron concentrations (for $Cc < 0.75$ mM), Φ is small enough (see the Section 2 of the supplementary materials) to approximate (6):

$$\Phi_{N_{Sat}} \approx N_{Sat}\Phi. \quad (7)$$

As Φ is linear with Cc at low SPM particle concentration (see Fig. 3a of [31]), $\Phi_{N_{Sat}}$ is also proportional to Cc and N_{Sat} at low concentrations (for $Cc < 0.75$ mM).

For large values of N_{Sat} ($N_{Sat} > 5$), Eq. (6) shows that the increase of $\Phi_{N_{Sat}}$ with N_{Sat} becomes less important. Indeed for typical values of Φ (~0.15), $\Phi_{N_{Sat}} \approx 0.48$ for $N_{Sat} = 4$. To reach $\Phi_{N_{Sat}} \approx 0.7$, one should use 8 saturation pulses. Increasing the number of saturation pulses would present several drawbacks, as an increase of the Specific Absorption Rate (SAR) but also a partial recovery of the saturated signal during the train of saturation pulses if this latter is too long. Moreover, artifacts become more important when N_{Sat} increases. Therefore, we estimate that the optimum value of N_{Sat} is 3.

If condition (4) is not verified, protons can be considered as static compared to the SPM particles size. Therefore, all the N_{Sat} saturation pulses will saturate the same protons, which

involves $\Phi_{N_{Sat}} = \Phi$. In this case, using several saturation pulses is useless.

An analytical expression of the contrast produced by the modified ORS sequence can be obtained. The only difference between the modified ORS sequence and the ORS sequence is the number of saturation pulses. As this only affects the fraction of saturated protons (the saturation pulses are applied before the imaging sequence), the contrast is simply obtained by changing the fraction of saturated protons in Eq. (3), Φ, by $\Phi_{N_{Sat}}$ Eq. (6). The contrast generated by the modified ORS sequence is thus given by

$$C = \Phi_{N_{Sat}}(\omega_0, \Delta\omega, B_{eq}, Cc) \sin \alpha M_z^0 e^{-TE(r_2^* Cc + R_2^*)}. \quad (8)$$

By comparing Eqs. (8) and (3), we see that the influence of the SPM particle concentration, the particles relaxivity, the echo time, ω_0 and $\Delta\omega$ on the contrast will be the same as observed for the classical ORS sequence studied in [31]. The only difference is the introduction of a new parameter: N_{Sat} (Δt_{Sat} does not influence the contrast if condition (4) is fulfilled). As $\Phi_{N_{Sat}}$ increases with N_{Sat} and as the contrast is proportional to $\Phi_{N_{Sat}}$, the contrast must increase with N_{Sat}. Moreover, Eq. (7) indicates that the contrast is proportional to N_{Sat} at low SPM particle concentration.

Note that the noise is not introduced in (8). However, it must be taken into account to compare the theoretical predictions to the Contrast to Noise Ratio (CNR) measured on the experimental MR images. In this work, the prediction calculated with Eq. (8) is multiplied by a constant corrective factor (which is the same for all the experiments) for the comparison with experiments, in order to take the noise into account. In addition to the noise, the corrective factor must also take into account the proton density, which is a constant multiplying the contrast value. The proton density is present in Eq. (8) through M_z^0. The comparison between theory and simulations is straightforward and no scaling factor has to be used.

3. Materials and methods

3.1. Phantoms

The phantoms are constituted of a 40 mm diameter tube filled with 1.5% agarose gel in which five 6 mm diameter tubes containing different concentrations of SPM particles dispersed in 1.5% agarose gel were embedded. The SPM particles used in this work were the 3 nm-VSOP and the 20 nm-VSOP from Ferropharm (Teltow, Germany). These particles were characterized in Ref. [27,31]. They are constituted of magnetite (Fe_3O_4) and their features are presented in Table 2. The relaxation times of the different samples can be calculated thanks to the relaxivities provided in Table 2.

The relaxation times of the agarose gels ($T_1 = 3$ s and $T_2 = 80$ ms) were measured as described in [27,31] at 11.7 T.

Table 2
SPM particles properties [27,31]. The relaxivity measurements were performed with the MRI scanner at 11.7 T. The equatorial field was measured with magnetometry. The relaxation rates of the different samples can be calculated with the following equation $1/T_1 = r_1 Cc + (1/T_1)_{agarose}$ and $1/T_2^* = r_2^* Cc + (1/T_2^*)_{agarose}$.

Particles	r_1 ($mM^{-1}\,s^{-1}$)	r_2^* ($mM^{-1}\,s^{-1}$)	Mono-crystal radius (nm)	B_{eq} (T)
3 nm-VSOP	2.1	90	3.74	0.13
20 nm-VSOP	2.1	200	4.21	0.13

3.2. MRI experiments

MR images were acquired on a 11.7 T scanner (Bruker, Biospec, Ettlingen, Germany) with a quadrature volume coil (inner diameter of 40 mm). The image acquisition sequence was a Fast Imaging with Steady-state Precession (FISP) [1–3,46,47,53]. Two images were acquired and subtracted pixel by pixel to obtain the ORS image. The first image was acquired without saturation pulses. The second one was acquired with the application of N_{Sat} saturation pulses before the FISP sequence.

The modified ORS-FISP sequence parameters were TR = 4 ms, TE = 1.5 ms, flip angle = 10°, $\Delta t_{Sat} = 5$ ms, matrix size = 128 × 128, slice thickness = 2 mm, FOV = 40 mm, four segments and a number of averages of 20. The saturation pulses were sinc pulses with 3 lobes and a flip angle of 90°. All the saturation pulses were followed by a rectangular spoiler gradient. If they are not mentioned, the saturation pulse parameters were $\omega_0 = 250$ Hz and $\Delta\omega = 400$ Hz. Our previous work showed that these saturation pulse parameters were the best compromise for an optimal ORS contrast [31]. The total duration of the saturation pulse was about 15 ms while the central peak of the sinc pulse had a width of maximum 2 ms.

T_2-weighted RARE (Rapid Acquisition with Relaxation Enhancement) images were acquired with TR/TE = 1500/15 ms and a RARE factor of 4.

The Contrast to Noise Ratio (CNR) was measured on the ORS image which is obtained by the subtraction of the MR image realized with the saturation pulses from the one obtained without saturation. The CNR between two regions of the ORS image with and without particles was calculated with [1,2]

$$\mathrm{CNR} = \frac{S_{ORS,SPM} - S_{ORS,\,\text{without SPM}}}{\sigma_0}, \quad (9)$$

where σ_0 is the standard deviation of the void, $S_{ORS,SPM}$ and $S_{ORS,\,\text{without SPM}}$ are the signals measured on the ORS image in a region with and without SPM particles respectively. The Region Of Interest (ROI) was placed manually on a homogeneous area. The results shown in graphs were expressed as mean CNR ± the standard deviation calculated from 3 measurements of CNR on different ROIs. The image processing was performed with ImageJ (National Institutes of Health, Bethesda, USA) and the graphs were plotted using the Matplotlib library of Python.

3.3. Simulations

Numerical simulations were performed to study the contrast induced by the modified ORS-FISP sequence. They simulate the NMR signal of protons in the presence of magnetic particles when submitted to the modified ORS-sequence. These simulations allowed to compute the contrast between a solution containing SPM particles and a solution without SPM particles. The simulation protocol used in this work was the same as used in [31] which studied the classical ORS-FISP sequence, except that several saturation pulses were applied before the imaging sequence application.

The simulations parameters were, if not explicitly mentioned,

- Temperature: 310 K (human body temperature).
- Water proton diffusion coefficient: $D = 3 \cdot 10^{-9}$ m^2 s^{-1}.
- SPM particles (magnetite) magnetization: 100 A m^2/kg [Fe], corresponding to B_{eq} = 0.16 T.
- SPM particle radius: 10 nm.
- Relaxation times of the solution containing the SPM particles (agarose gel): T_1 = 3 s and T_2 = 80 ms.
- Time between the saturation pulses: $\Delta t_{Sat} = 5$ ms.
- Saturation pulses parameters: $\omega_0 = 250$ Hz and $\Delta\omega = 400$ Hz.
- Number of saturation pulses N_{Sat}: from 1 to 6.

– Iron concentration Cc: from 0 to 1 mM.

The calculation of the longitudinal relaxivity at 11.7 T for these particles characteristics provides a value of $r_1 = 0.4\,\mathrm{mM}^{-1}\,\mathrm{s}^{-1}$ which is rather small. This is due to the large radius of the particles that moves the T_1 dispersion to the small magnetic fields. In our simulations, the longitudinal relaxivity is supposed to be null which is thus a reasonable assumption. The calculation of the transverse relaxivity gives $r_2^* = 330\,\mathrm{mM}^{-1}\,\mathrm{s}^{-1}$.

The data presented in this work were obtained by averaging the results of three simulations. The contrast presented on graphs corresponds to the mean ± the standard deviation of three measurements. As for the theory, the noise was not taken into account in the simulations. The proton density was scaled to 1 in the simulation. Therefore, the contrast obtained with simulations was comprised between 0 and 1.

All the routines were written in C++, parallelized with OPENMP and used the GNU Scientific Library (GSL). The simulations were performed on the resources of the *Consortium des Equipements de Calcul Intensif* (CECI). Data analysis and graphs were performed with Python with the Numpy, Scipy and Matplotlib libraries.

3.4. Quantification of the agreement between simulations, experiment and theory

First it should be mentioned that the direct and simultaneous comparison between theory, simulation results and experimental results is almost impossible. The comparison between the simulations and the experimental results is not straightforward since the particle characteristics used in the simulations cannot perfectly match the real particles characteristics. This is why we decided to first compare theory with simulations and then compare theory with experimental results.

The agreement between the simulation and the theoretical predictions was quantified by the calculation of the coefficient of determination R^2. To compute R^2, graphs representing the simulation data as a function of the theoretical predictions were first plotted. The resulting curve should show a linear relationship with a slope equal to 1. The coefficient of determination was calculated as described in [54]

$$R^2 = 1 - \frac{\sum_{i=1}^{n}(y_i - \hat{y}_i)^2}{\sum_{i=1}^{n}(y_i - \bar{y})^2}, \tag{10}$$

where y_i are the experimental (or simulation) values of the contrast, $\hat{y}_i$ are the theoretical values of the contrast and $\bar{y} = \frac{1}{n}\sum_{i=1}^{n} y_i$ is the mean of the experimental (or simulation) values. A coefficient equal to 1 would indicate a perfect regression. For the evaluation of the agreement between theory and experiment, first a fitting of experimental data by the theory was performed, using a single adjustable parameter which allows to take the noise and the proton density into account, as previously done in [31]. Then, the values of the experimental data were plotted versus the scaled theoretical predictions and the coefficient of determination was computed as described above.

4. Results

4.1. Theoretical and simulation results

Numerical simulations were first computed to study the influence of the SPM particle concentration and the saturation pulse number N_{Sat} on the contrast (Fig. 3).

Fig. 3a shows the influence of the SPM particles concentration Cc on the contrast for different N_{Sat} values. The simulation results and the theoretical predictions are compared on this graph. The theoretical predictions were calculated with Eq. (8) using the simulation parameters (Section 3.3). Both simulation and theoretical results showed a contrast increase with N_{Sat} for all concentrations. This behavior is corroborated by Fig. 3b, which shows the influence of N_{Sat} on the contrast for different SPM particle concentrations. Indeed, this graph clearly shows an increase of the contrast with N_{Sat}. A good agreement between simulations and theory can be observed in Fig. 3a and b (R^2 = 0.94 and 0.96).

The increase of the contrast with N_{Sat} is predicted by the theory (Section 2.2). Indeed, Eq. (8) shows that the contrast dependence on N_{Sat} is only contained in the fraction of saturated protons $\Phi_{N_{Sat}}$. As the contrast is proportional to $\Phi_{N_{Sat}}$ (Eq. (8)), and as $\Phi_{N_{Sat}}$ increases with N_{Sat} (Eq. (6)), the contrast logically increases with the increase of the number of saturation pulses.

The graph 3a shows that the influence of the particle concentration on the contrast is the same as observed in Ref. [31]. Indeed, the contrast first increases linearly with Cc, reaches a maximum and then decreases. This can be understood using Eq. (8). At low concentration, the exponential term of Eq. (8) does not depend on Cc ($e^{-TE(r_2^* Cc + R_2^*)} \approx e^{-R_2^* TE}$), which implies that Cc influences the contrast only through Φ_{NSat}. As in this case $\Phi_{NSat} \approx N_{Sat}\Phi$ (Eq. (7)) and Φ is proportional to Cc [31], the contrast is linearly dependent on Cc. At high concentration, the exponential term of Eq. (8) dominates the contrast behavior. This leads to a contrast decrease with Cc at high SPM particles concentration.

4.2. Experimental results

MR images of phantoms containing 20 nm-VSOP in different concentrations obtained with different numbers of saturation pulse are show in Fig. 4a. The contrast clearly increased with N_{Sat} and the particle concentration Cc, as predicted by simulations and theory (Fig. 3).

The CNR extracted from phantoms and theoretical predictions were plotted in Fig. 4b and c. The theoretical predictions were calculated with Eq. (8) using the experimental parameters of the 20 nm-VSOP (Table 2) and of the MRI sequence. These predictions were then scaled by the same corrective factor in order to take into account the noise and the protons density.

The influence of the SPM particle concentration is shown in Fig. 4b. A good agreement was observed between experiments and theory (R^2 = 0.9). The contrast dependence on Cc and N_{Sat} was the same as predicted by the numerical simulations (Fig. 3a). Indeed, the CNR increased with N_{Sat} for all Cc. For all N_{Sat} values, the CNR increased linearly with Cc until a maximum was reached. The decrease of the CNR observed for the simulations at high values of Cc in Fig. 3a, is not observed here because the SPM particle concentration was not high enough.

Fig. 4c directly shows the influence of N_{Sat} on the contrast. An increase of the contrast with N_{Sat} is observed for all SPM particle concentrations, as predicted by theory. The experimental data were in good agreement with the theoretical predictions (R^2 = 0.9) and the simulation results (Fig. 3b). The same contrast behavior was observed with the 3 nm-VSOP SPM particles (Fig. S2).

4.3. Influence of ω_0 on the contrast

Fig. 5 shows the influence of N_{Sat} on the contrast for two values of the saturation pulse frequency offset ω_0.

The numerical simulations results and the theoretical predictions are presented in Fig. 5a (R^2 = 0.97). The SPM particle concentration was fixed at 0.3 mM [Fe]. This graph shows that the contrast decreases with the increase of ω_0 for all N_{Sat} values.

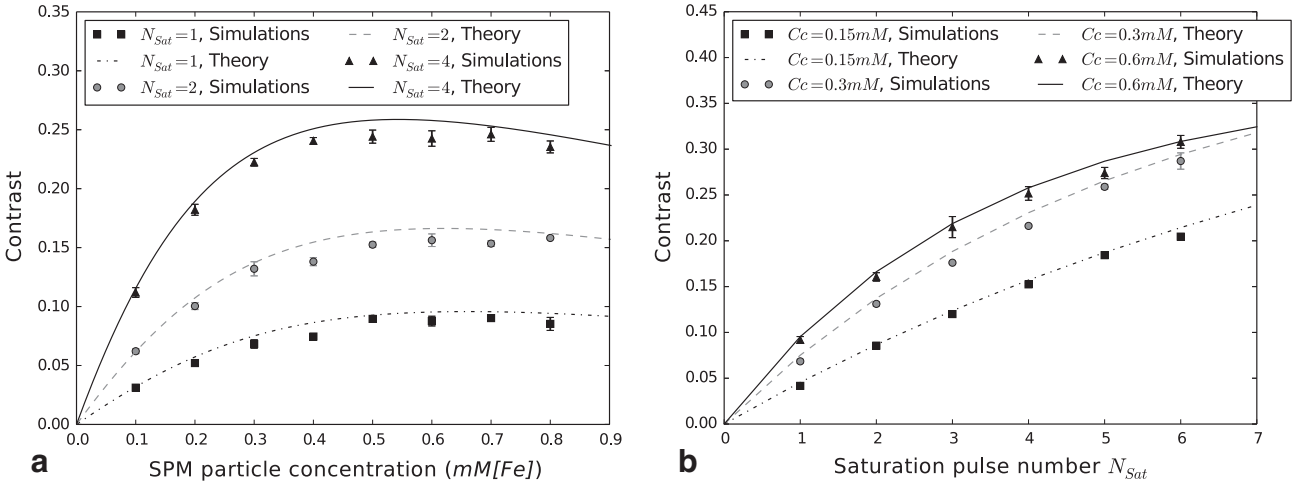

Fig. 3. Comparison of numerical simulations and theory. (a) Influence of the SPM particle concentration (expressed in mM [Fe]) on the contrast for different N_{Sat} values. (b) Influence of N_{Sat} on the contrast for different SPM particle concentrations.

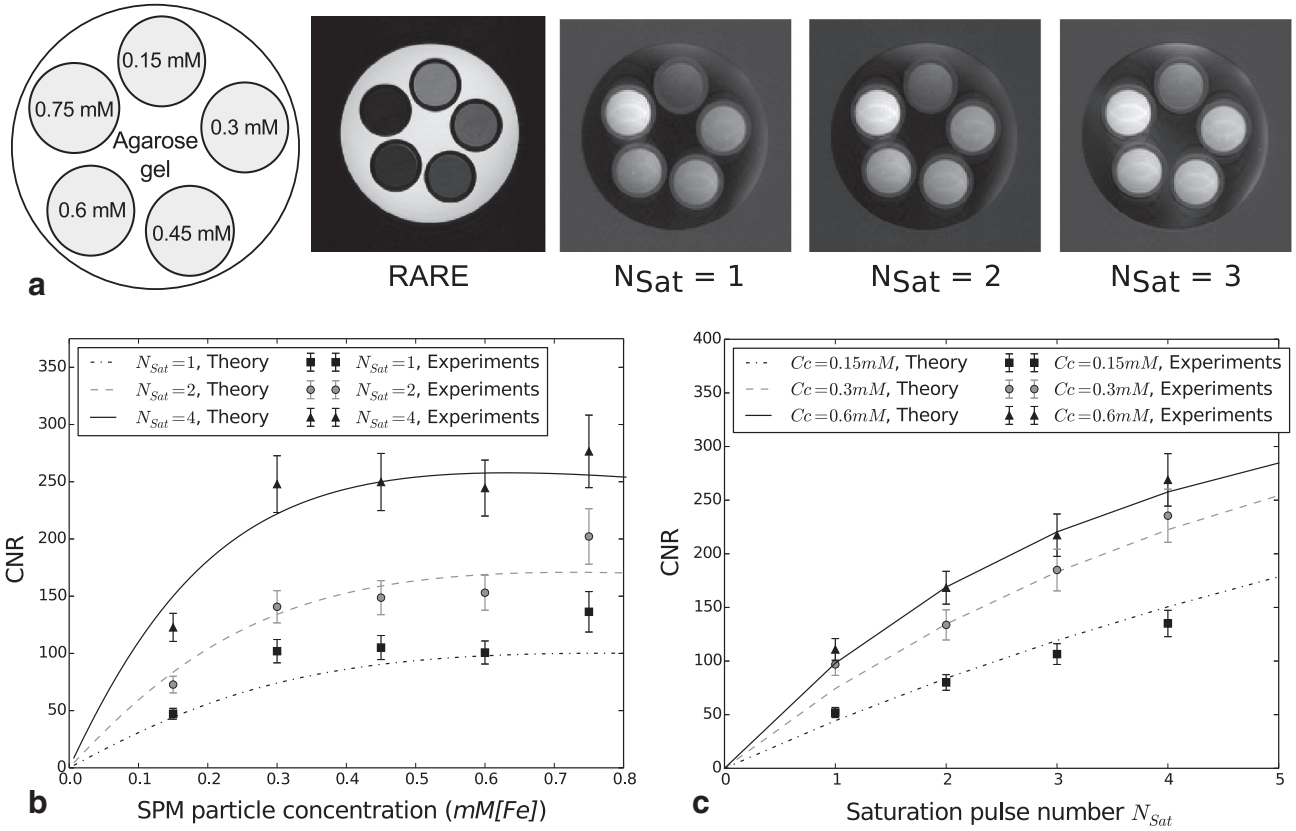

Fig. 4. (a) MR images of a phantom containing 20 nm-VSOP in different SPM particle concentrations. These images were obtained with different number of saturation pulses. (b and c) Comparison of the CNR extracted from the images and the theoretical predictions calculated with Eq. (8). (b) Influence of the SPM particle concentration on the contrast for different N_{Sat} values. (c) Influence of N_{Sat} on the contrast for different particle concentrations.

MR images of a phantom containing 20 nm-VSOP obtained with ORS sequences using $N_{Sat} = 3$ and different ω_0 values are presented in Fig. 5b. These images confirm the results obtained by numerical simulation and theory. Indeed, they show that the contrast decreases with the increase of ω_0, as predicted by theory and simulations (Fig. 5a).

The CNR extracted from phantom presented in Fig. 5b for Cc = 0.3 mM [Fe] and the corresponding theoretical predictions are plotted in Fig. 5c. This figure shows a contrast decrease with the increase of ω_0 for all values of N_{Sat}. The experimental values were in good agreement with theory (R^2 = 0.88) and simulations (Fig. 5a). The same contrast behavior was also observed with the 3 nm-VSOP SPM particles (see Fig. S3 of the supplementary materials).

The contrast decrease with the increase of ω_0 was already observed and explained in Ref. [31] for $N_{Sat} = 1$. These explanations can extended for all values of N_{Sat} thanks to Eq. (8) which shows that the contrast only depends on ω_0 through the fraction of saturated

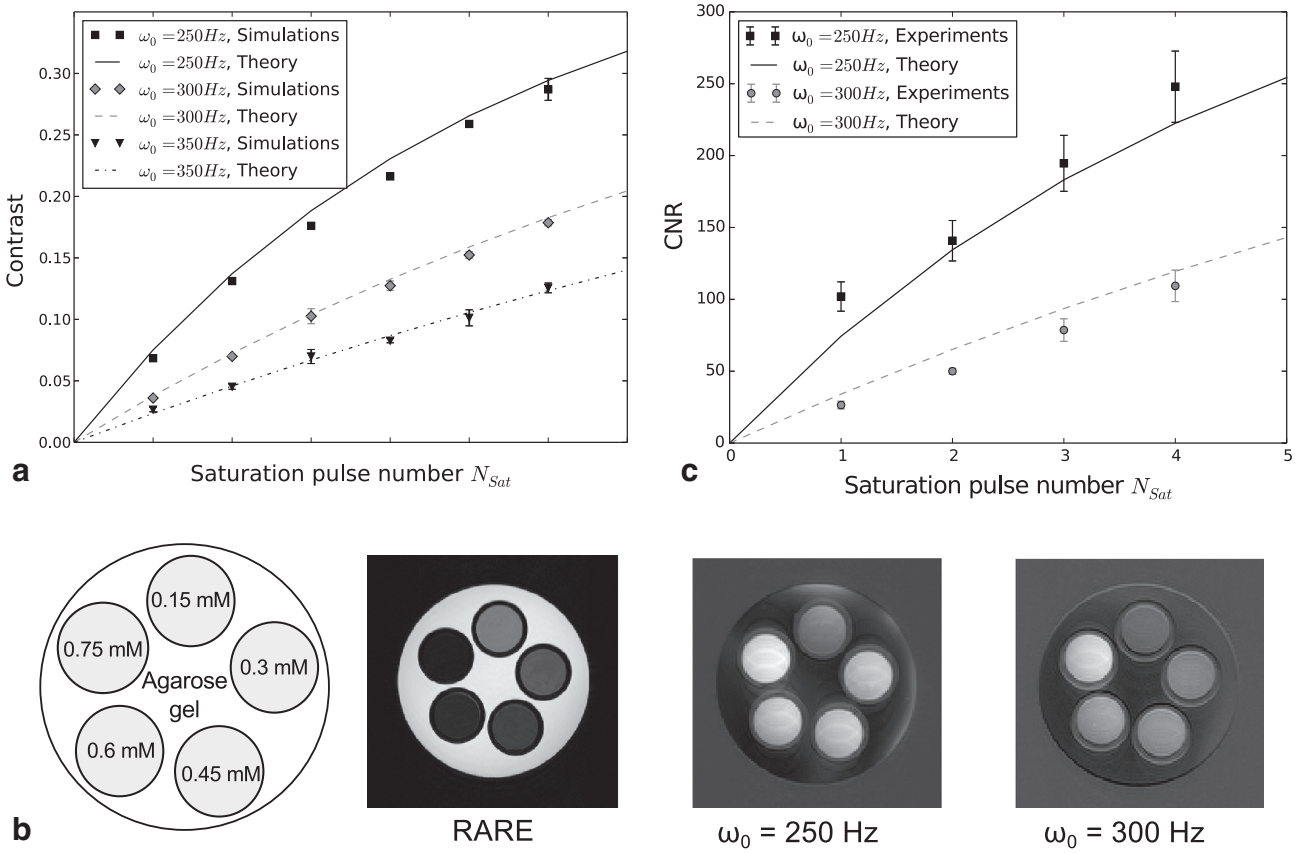

Fig. 5. Influence of N_{sat} on the contrast for different values of ω_0: numerical simulations, experiments and their comparison with theory. (a) Numerical simulation results obtained with Cc = 0.3 mM [Fe]. (b) MR images of a phantom containing 20 nm-VSOP obtained with a RARE and the ORS sequence using $N_{Sat} = 3$ and two different ω_0 values. (c) Influence of N_{Sat} on the CNR extracted from the MR images. The SPM particle concentration was fixed at 0.3 mM [Fe].

protons $\Phi_{N_{Sat}}$. It was demonstrated in [31] that Φ decreases with the increase of ω_0. Therefore, Eq. (6) implies that $\Phi_{N_{Sat}}$ decreases with the increase of ω_0. As contrast is proportional to $\Phi_{N_{Sat}}$ (Eq. (8)), the contrast must decreases with the increase of ω_0.

As Φ also decreases with the decrease of $\Delta\omega$, a decrease of $\Delta\omega$ also implies a contrast decrease. This behavior is shown in Fig. S4 for the 3 nm-VSOP particles. Simulation results obtained for three values of $\Delta\omega$ and for 20 nm particles were also compared to our theory in Fig. S5.

5. Discussion

First it should be mentioned that the contrast observed in the ORS images cannot be attributed to Magnetization Transfer between agarose protons and free water protons. Indeed such a mechanism would have led to a brighter zone in the larger tube containing only agarose gel, without SPM particles, which was not observed in our ORS images. In the present work, the ORS sequence was improved by adding several saturation pulses before the imaging sequence, while only one saturation pulse is used in the classical ORS sequence studied in [28,29,31,55]. The results showed that this simple procedure significantly increased the contrast. A theoretical description of the modified ORS sequence was provided. An analytical expression of the contrast able to predict the contrast in function of the sequence parameters was obtained. This expression was derived considering that the protons were efficiently mixed between the saturation pulses. This is the case when considering non aggregated particles. But when clusters are present, as it is often the case in vivo, one must reevaluate the minimum value of Δt_{sat} with the aggregate radius instead of the particle radius. For example, for a 500 nm cluster in water, Δt_{sat} must be larger than 3.8 ms. Therefore, for such large clusters, longer interpulse delays would have to be used in order remain in the validity domain of the theory. Clustering may also influence the transverse relaxivity r_2^* of the particles, which will affect the contrast through the exponential term of Eq. (8). This will have to be taken into account for future in vivo applications.

When the mixing of protons between saturation pulses is efficient, the theoretical model showed that the only difference between the classical and the modified ORS sequence was the fraction of saturated protons, which increases with the saturation pulse number. As the contrast is proportional to the fraction of saturated protons, this implies that the contrast increases with the saturation pulses number. Logically, the influence of the other parameters (Cc, $\Delta\omega$, ω_0) is at least qualitatively similar to what was previously reported [31] for a "classical" ORS-sequence using a single saturation pulse.

The modified ORS sequence was also studied with numerical simulations and experiments carried out on agarose gel phantom on a 11.7 T MRI scanner. All the results were compared with the theoretical predictions. A good agreement between experiments, simulations and theory was observed. The theory can thus be used to predict the actual contrast.

The results first showed that the contrast increases with the saturation pulse number N_{Sat}, as expected. Therefore, increasing N_{Sat} seems to be a good way to increase the contrast. However, increasing N_{Sat} can also produce artifacts due to the field inhomogeneities, as seen on the phantoms of Fig. 4 (see the phantom edges). Therefore, even if the increase of N_{Sat} increases the contrast, the

choice of N_{Sat} must result from a compromise between the level of contrast (reflecting the sensitivity) and the contrast specificity. Our work shows that a value of 3 for N_{Sat} seems to be a good compromise. Larger values ineluctably led to the formation of artifacts. However, the optimum value of N_{Sat} will surely depends on the MRI scanner since it is directly related to the magnetic field inhomogeneities. However, one may expect that in vivo the value of N_{Sat} should be kept at 2, since artifacts are more likely to appear. But even with $N_{Sat} = 2$, the contrast will be significantly improved (by almost a factor of 2) as shown by our results. Of course, this will have to be confirmed by in vivo experiments.

The results also revealed that the influence on the contrast of the SPM particle concentration Cc is the same as observed for the classical ORS sequence (see Figs. 3 and 4 in [31]). Indeed, the contrast first linearly increases with Cc until a maximum is reached and then decreases. Therefore, there is an optimal SPM particle concentration to reach a maximum contrast.

The influence on the contrast of the saturation pulse parameters ω_0 and $\Delta\omega$ seems similar to what was previously observed for the classical ORS sequence (see Figs. 4 and 5 in [31]). Indeed the results obtained in the present work for two different values of ω_0 and $\Delta\omega$ (see Figs. 5, S3 and S4) showed that the contrast decreases with the increase of ω_0 and the decrease of $\Delta\omega$. As ω_0 and $\Delta\omega$ only affect the contrast through Φ, and as the contrast is proportional to $\Phi_{N_{Sat}}$ (Eq. (8)), the maximal contrast value is reached when Φ is maximum. As discussed in [31], this is the case for high value of $\Delta\omega$ and when $|\omega_0| \rightarrow \Delta\omega/2$. However, ω_0 must be high enough to avoid erroneous positive contrast created by the instrumental field inhomogeneities.

The influence of the SPM particle transverse relaxivity r_2^* and of the echo time TE on the contrast has not been studied in this work. These parameters do not affect the total fraction of saturated protons (see Eq. (8)). Therefore, their influence on the contrast must be similar as what was observed in [31], i.e. the contrast decreases exponentially with r_2^* and TE. These features indicate that SPM particles with low transverse relaxivity and a small echo time must be preferred for the modified ORS sequence.

The proposed sequence presents the disadvantage of using more pulses than the usual ORS sequence, which could cause an increase of SAR. However, the saturation pulses are only used once before the acquisition of the image. The small excitation angles (10°) used in the FISP sequence also ensures a normal SAR even if the repetition time is very small ($TR = 4$ ms). A comparison of the power dissipated during the FISP and the RARE sequences used in this work (taking into account the fact that SAR depends on the square of the pulse angle) shows that SAR of both sequences is approximately the same, as far as the number of saturation pulses is smaller than 6.

Finally, it should be mentioned that the saturation pulses used in this work (sinc3 pulse) can be considered as 'short' pulses which renders the comparison with the simulations and the theory rather easy. Another choice could have been to use several longer pulses or even a single continuous saturation pulse. In that case diffusion occurs during the pulse, which will influence the contrast, but in a non linear fashion as shown by Zurkiya and Hu [28] who reported an influence of the diffusion coefficient on the ORS contrast when using a continuous saturation pulse. In that case, the mixing of protons is occurring during the saturation pulse, and fast diffusion from protons inside the saturation shell to the outside of this shell is required. But on the other hand slow diffusion allows a larger residence time in the saturation shell and therefore a larger saturation angle resulting in a more efficient saturation. To describe such a saturation scheme, the simulation protocol and the theoretical modeling would have to be completely modified, which was beyond the scope of this work.

6. Conclusions

This work has presented a simple way to improve the ORS sequence in order to increase the contrast: using several saturation pulses before the imaging sequence. The modified ORS sequence was studied with numerical simulations and experiments on agarose gels. An analytical expression able to predict the contrast in function of the sequence and the SPM particles parameters was provided. The theoretical predictions were in good agreement with both simulation and experimental results.

It was clearly shown that the contrast increases with the number of saturation pulses. However, large N_{Sat} values results in artifacts affecting the contrast specificity. In this work the optimal number of saturation pulses was $N_{Sat} = 3$ even if in vivo this value may have to be decreased to 2 since artifacts are more likely to appear. Further investigations should be carried out to adapt the modified ORS sequence for in vivo applications since many phenomena (like particles clustering, altered diffusion properties, compartmentalization of water...) may affect contrast in vivo. These will have to be included in the theoretical modeling of the contrast induced by the modified ORS-sequence.

Appendix A. Supplementary material

Supplementary data associated with this article can be found, in the online version, at http://dx.doi.org/10.1016/j.jmr.2016.02.002.

References

[1] M.A. Bernstein, Handbook of MRI Pulse Sequences, Academic Press, Amsterdam, Boston, 2004.
[2] E.M. Haacke, R.W. Brown, M.R. Thompson, R. Venkatesan, Magnetic Resonance Imaging: Physical Principles and Sequence Design, first ed., Wiley-Liss, New York, 1999.
[3] Z.-P. Liang, P.C. Lauterbur, Principles of Magnetic Resonance Imaging: A Signal Processing Perspective, SPIE Optical Engineering Press; IEEE Press, Bellingham, WA; New York, 2000.
[4] Y. Gossuin, A. Hocq, P. Gillis, Q.L. Vuong, Physics of magnetic resonance imaging: from spin to pixel, J. Phys. Appl. Phys. 43 (2010), http://dx.doi.org/10.1088/0022-3727/43/21/213001.
[5] H. Shokrollahi, Contrast agents for MRI, Mater. Sci. Eng., C 33 (2013) 4485–4497, http://dx.doi.org/10.1016/j.msec.2013.07.012.
[6] G.-P. Yan, L. Robinson, P. Hogg, Magnetic resonance imaging contrast agents: overview and perspectives, Radiography 13 (2007) e5–e19, http://dx.doi.org/10.1016/j.radi.2006.07.005.
[7] Y. Gossuin, P. Gillis, A. Hocq, Q.L. Vuong, A. Roch, Magnetic resonance relaxation properties of superparamagnetic particles, Wiley Interdiscip. Rev. Nanomed. Nanobiotechnol. 1 (2009) 299–310.
[8] Q.L. Vuong, Y. Gossuin, P. Gillis, S. Delangre, New simulation approach using classical formalism to water nuclear magnetic relaxation dispersions in presence of superparamagnetic particles used as MRI contrast agents, J. Chem. Phys. 137 (2012), http://dx.doi.org/10.1063/1.4751442.
[9] Y.X. Wang, S.M. Hussain, G.P. Krestin, Superparamagnetic iron oxide contrast agents: physicochemical characteristics and applications in MR imaging, Eur. Radiol. 11 (2001) 2319–2331, http://dx.doi.org/10.1007/s003300100908.
[10] Z.R. Stephen, F.M. Kievit, M. Zhang, Magnetite nanoparticles for medical MR imaging, Mater. Today Kidlington Engl. 14 (2011) 330–338, http://dx.doi.org/10.1016/S1369-7021(11)70163-8.
[11] C. Corot, P. Robert, J.-M. Idée, M. Port, Recent advances in iron oxide nanocrystal technology for medical imaging, Adv. Drug Delivery Rev. 58 (2006) 1471–1504, http://dx.doi.org/10.1016/j.addr.2006.09.013.
[12] J. Kolosnjaj-Tabi, C. Wilhelm, O. Clément, F. Gazeau, Cell labeling with magnetic nanoparticles: opportunity for magnetic cell imaging and cell manipulation, J. Nanobiotechnol. 11 (2013) S7.
[13] W.J. Rogers, C.H. Meyer, C.M. Kramer, Technology insight: in vivo cell tracking by use of MRI, Nat. Clin. Pract. Cardiovasc. Med. 3 (2006) 554–562, http://dx.doi.org/10.1038/ncpcardio0659.
[14] J. Cai, X. Zhang, X. Wang, C. Li, G. Liu, In vivo MR imaging of magnetically labeled mesenchymal stem cells transplanted into rat liver through hepatic arterial injection, Contrast Media Mol. Imaging 3 (2008) 72–77, http://dx.doi.org/10.1002/cmmi.231.
[15] A. Luciani, S. Dechoux, V. Deveaux, M. Poirier-Quinot, N. Luciani, M. Levy, S. Ballet, S. Manin, C. Péchoux, G. Autret, O. Clément, A. Rahmouni, A. Mallat, C. Wilhelm, S. Lotersztajn, F. Gazeau, Adipose tissue macrophages: MR tracking to monitor obesity-associated inflammation, Radiology 263 (2012) 786–793.

[16] J.W.M. Bulte, D.L. Kraitchman, Iron oxide MR contrast agents for molecular and cellular imaging, NMR Biomed. 17 (2004) 484–499, http://dx.doi.org/10.1002/nbm.924.
[17] A.A.M. Elsherbini, A. El-Shahawy, Effect of SPIO nanoparticle concentrations on temperature changes for hyperthermia via MRI, J. Nanomater. 2013 (2013), http://dx.doi.org/10.1155/2013/467878.
[18] B. Blasiak, F.C.J.M. van Veggel, B. Tomanek, Applications of nanoparticles for MRI cancer diagnosis and therapy, J. Nanomater. 2013 (2013) 1–12, http://dx.doi.org/10.1155/2013/148578.
[19] X.-H. Peng, X. Qian, H. Mao, A.Y. Wang, Targeted magnetic iron oxide nanoparticles for tumor imaging and therapy, Int. J. Nanomed. 3 (2008) 311.
[20] N. Schleich, P. Sibret, P. Danhier, B. Ucakar, S. Laurent, R.N. Muller, C. Jérôme, B. Gallez, V. Préat, F. Danhier, Dual anticancer drug/superparamagnetic iron oxide-loaded PLGA-based nanoparticles for cancer therapy and magnetic resonance imaging, Int. J. Pharm. 447 (2013) 94–101, http://dx.doi.org/10.1016/j.ijpharm.2013.02.042.
[21] C. Sun, J.S.H. Lee, M. Zhang, Magnetic nanoparticles in MR imaging and drug delivery, Adv. Drug Delivery Rev. 60 (2008) 1252–1265, http://dx.doi.org/10.1016/j.addr.2008.03.018.
[22] E.-J.P.A. Vonken, M. Schär, J. Yu, C.J.G. Bakker, M. Stuber, Direct in vitro comparison of six three-dimensional positive contrast methods for susceptibility marker imaging, J. Magn. Reson. Imaging 38 (2013) 344–357, http://dx.doi.org/10.1002/jmri.23976.
[23] W. Liu, H. Dahnke, E.K. Jordan, T. Schaeffter, J.A. Frank, In vivo MRI using positive-contrast techniques in detection of cells labeled with superparamagnetic iron oxide nanoparticles, NMR Biomed. 21 (2008) 242–250, http://dx.doi.org/10.1002/nbm.1187.
[24] C. Lin, S. Cai, J. Feng, Positive contrast imaging of SPIO nanoparticles, J. Nanomater. 2012 (2012) 1–9, http://dx.doi.org/10.1155/2012/734842.
[25] M. Stuber, W.D. Gilson, M. Schär, D.A. Kedziorek, L.V. Hofmann, S. Shah, E.J. Vonken, J.W. Bulte, D.L. Kraitchman, Positive contrast visualization of iron oxide-labeled stem cells using inversion-recovery with ON-resonant water suppression (IRON), Magn. Reson. Med. 58 (2007) 1072–1077.
[26] G. Korosoglou, L. Tang, D. Kedziorek, K. Cosby, W.D. Gilson, E.-J. Vonken, M. Schar, D. Sosnovik, D.L. Kraitchman, R.G. Weiss, R. Weissleder, M. Stuber, Positive contrast MR-lymphography using inversion recovery with ON-resonant water suppression (IRON), J. Magn. Reson. Imaging 27 (2008) 1175–1180, http://dx.doi.org/10.1002/jmri.21337.
[27] S. Delangre, Q.L. Vuong, D. Henrard, J. Magat, C. Po, B. Gallez, Y. Gossuin, Theoretical and experimental study of ON-resonance saturation, an MRI sequence for positive contrast with superparamagnetic nanoparticles, J. Magn. Reson. (2015), http://dx.doi.org/10.1016/j.jmr.2015.01.007.
[28] O. Zurkiya, X. Hu, Off-resonance saturation as a means of generating contrast with superparamagnetic nanoparticles, Magn. Reson. Med. 56 (2006) 726–732, http://dx.doi.org/10.1002/mrm.21024.
[29] C. Khemtong, C.W. Kessinger, J. Ren, E.A. Bey, S.-G. Yang, J.S. Guthi, D.A. Boothman, A.D. Sherry, J. Gao, In vivo off-resonance saturation magnetic resonance imaging of v 3-targeted superparamagnetic nanoparticles, Cancer Res. 69 (2009) 1651–1658, http://dx.doi.org/10.1158/0008-5472.CAN-08-3231.
[30] P. Krämer, X. Helluy, T. Kampf, E. Lang, P.M. Jakob, Flow-enhanced off-resonance saturation for remote detection of iron-based contrast agents, Magn. Reson. Med. Off. J. Soc. Magn. Reson. Med. Soc. Magn. Reson. Med. 63 (2010) 1708–1715, http://dx.doi.org/10.1002/mrm.22354.
[31] S. Delangre, Q.L. Vuong, D. Henrard, C. Po, B. Gallez, Y. Gossuin, Bottom-up study of the MRI positive contrast created by the off-resonance saturation sequence, J. Magn. Reson. (2015).
[32] C.H. Cunningham, T. Arai, P.C. Yang, M.V. McConnell, J.M. Pauly, S.M. Conolly, Positive contrast magnetic resonance imaging of cells labeled with magnetic nanoparticles, Magn. Reson. Med. 53 (2005) 999–1005, http://dx.doi.org/10.1002/mrm.20477.
[33] W. Foltz, C. Cunningham, A. Mutsaers, S. Conolly, D. Stewart, A. Dick, Positive-contrast imaging in the rabbit hind-limb of transplanted cells bearing endocytosed superparamagnetic beads, J. Cardiovasc. Magn. Reson. 8 (2006) 817–823, http://dx.doi.org/10.1080/10976640600777819.
[34] P. Balchandani, M. Yamada, J. Pauly, P. Yang, D. Spielman, Self-refocused spatial-spectral pulse for positive contrast imaging of cells labeled with SPIO nanoparticles, Magn. Reson. Med. 62 (2009) 183–192, http://dx.doi.org/10.1002/mrm.21973.
[35] J.-H. Seppenwoolde, M.A. Viergever, C.J.G. Bakker, Passive tracking exploiting local signal conservation: the white marker phenomenon, Magn. Reson. Med. 50 (2003) 784–790, http://dx.doi.org/10.1002/mrm.10574.
[36] V. Mani, K.C. Briley-Saebo, V.V. Itskovich, D.D. Samber, Z.A. Fayad, Gradient echo acquisition for superparamagnetic particles with positive contrast (GRASP): sequence characterization in membrane and glass superparamagnetic iron oxide phantoms at 1.5 T and 3 T, Magn. Reson. Med. 55 (2006) 126–135, http://dx.doi.org/10.1002/mrm.20739.
[37] J.-H. Seppenwoolde, K.L. Vincken, C.J.G. Bakker, White-marker imaging—separating magnetic susceptibility effects from partial volume effects, Magn. Reson. Med. 58 (2007) 605–609, http://dx.doi.org/10.1002/mrm.21304.
[38] V. Mani, E. Adler, K.C. Briley-Saebo, A. Bystrup, V. Fuster, G. Keller, Z.A. Fayad, Serial in vivo positive contrast MRI of iron oxide-labeled embryonic stem cell-derived cardiac precursor cells in a mouse model of myocardial infarction, Magn. Reson. Med. Off. J. Soc. Magn. Reson. Med. Soc. Magn. Reson. Med. 60 (2008) 73–81, http://dx.doi.org/10.1002/mrm.21642.
[39] P.R. Seevinck, H. de Leeuw, C. Bos, C.J.G. Bakker, Highly localized positive contrast of small paramagnetic objects using 3D center-out radial sampling with off-resonance reception, Magn. Reson. Med. 65 (2011) 146–156, http://dx.doi.org/10.1002/mrm.22594.
[40] H. Zhu, K. Demachi, M. Sekino, Phase gradient imaging for positive contrast generation to superparamagnetic iron oxide nanoparticle-labeled targets in magnetic resonance imaging, Magn. Reson. Imaging 29 (2011) 891–898, http://dx.doi.org/10.1016/j.mri.2011.04.011.
[41] Q. Zhao, J. Langley, S. Lee, W. Liu, Positive contrast technique for the detection and quantification of superparamagnetic iron oxide nanoparticles in MRI, NMR Biomed. 24 (2011) 464–472, http://dx.doi.org/10.1002/nbm.1608.
[42] F. Eibofner, G. Steidle, R. Kehlbach, R. Bantleon, F. Schick, Positive contrast imaging of iron oxide nanoparticles with susceptibility-weighted imaging, Magn. Reson. Med. 64 (2010) 1027–1038.
[43] H. Dahnke, W. Liu, D. Herzka, J.A. Frank, T. Schaeffter, Susceptibility gradient mapping (SGM): a new postprocessing method for positive contrast generation applied to superparamagnetic iron oxide particle (SPIO)-labeled cells, Magn. Reson. Med. Off. J. Soc. Magn. Reson. Med. Soc. Magn. Reson. Med. 60 (2008) 595–603, http://dx.doi.org/10.1002/mrm.21478.
[44] L.A. Crowe, F. Ris, S. Nielles-Vallespin, P. Speier, S. Masson, M. Armanet, P. Morel, C. Toso, D. Bosco, T. Berney, J.-P. Vallée, A novel method for quantitative monitoring of transplanted islets of langerhans by positive contrast magnetic resonance imaging: 3D radial UTE MRI for iron oxide labeled islet cells, Am. J. Transplant. 11 (2011) 1158–1168, http://dx.doi.org/10.1111/j.1600-6143.2011.03559.x.
[45] O.M. Girard, J. Du, L. Agemy, K.N. Sugahara, V.R. Kotamraju, E. Ruoslahti, G.M. Bydder, R.F. Mattrey, Optimization of iron oxide nanoparticle detection using ultrashort echo time pulse sequences: comparison of T_1, T_2^*, and synergistic T_1–T_2^* contrast mechanisms, Magn. Reson. Med. 65 (2011) 1649–1660, http://dx.doi.org/10.1002/mrm.22755.
[46] A. Oppelt, R. Graumann, H. BarfuB, H. Fischer, W. Hartl, W. Schajor, FISP – a new fast MRI sequence, Electromedica 54 (1986) 15–18.
[47] Y. Zur, S. Stokar, P. Bendel, An analysis of fast imaging sequences with steady-state transverse magnetization refocusing, Magn. Reson. Med. 6 (1988) 175–193, http://dx.doi.org/10.1002/mrm.1910060206.
[48] W. Hänicke, H.U. Vogel, An analytical solution for the SSFP signal in MRI, Magn. Reson. Med. Off. J. Soc. Magn. Reson. Med. Soc. Magn. Reson. Med. 49 (2003) 771–775, http://dx.doi.org/10.1002/mrm.10410.
[49] E. Davies, Y. Huang, J.B. Harper, J.M. Hook, D.S. Thomas, I.M. Burgar, P.J. Lillford, Dynamics of water in agar gels studied using low and high resolution ^{1}H NMR spectroscopy, Int. J. Food Sci. Technol. 45 (2010) 2502–2507, http://dx.doi.org/10.1111/j.1365-2621.2010.02448.x.
[50] L. Filidoro, O. Dietrich, J. Weber, E. Rauch, T. Oerther, M. Wick, M.F. Reiser, C. Glaser, High-resolution diffusion tensor imaging of human patellar cartilage: feasibility and preliminary findings, Magn. Reson. Med. 53 (2005) 993–998, http://dx.doi.org/10.1002/mrm.20469.
[51] E. Kermarrec, J.-F. Budzik, C. Khalil, V. Le Thuc, C. Hancart-Destee, A. Cotten, In vivo diffusion tensor imaging and tractography of human thigh muscles in healthy subjects, AJR Am. J. Roentgenol. 195 (2010) W352–W356, http://dx.doi.org/10.2214/AJR.09.3368.
[52] R. Ward, S. Caruthers, C. Yablon, M. Blake, M. DiMasi, S. Eustace, Analysis of diffusion changes in posttraumatic bone marrow using navigator-corrected diffusion gradients, Am. J. Roentgenol. 174 (2000) 731–734, http://dx.doi.org/10.2214/ajr.174.3.1740731.
[53] M.L. Gyngell, The steady-state signals in short-repetition-time sequences, J. Magn. Reson. 1969 (81) (1989) 474–483, http://dx.doi.org/10.1016/0022-2364(89)90083-8.
[54] D.C. Montgomery, G.C. Runger, Applied Statistics and Probability for Engineers, Wiley, Hoboken, NJ, 2011.
[55] C. Khemtong, O. Togao, J. Ren, C.W. Kessinger, M. Takahashi, A.D. Sherry, J. Gao, Off-resonance saturation MRI of superparamagnetic nanoprobes: theoretical models and experimental validations, J. Magn. Reson. San Diego Calif 1997 (209) (2011) 53–60, http://dx.doi.org/10.1016/j.jmr.2010.12.013.